Interactions of semiflexible filaments and molecular motors

Dmitry Karpeev,[1] Igor S. Aranson,[2] Lev S. Tsimring,[3] and Hans G. Kaper[4,1]
[1]*Mathematics and Computer Science Division, Argonne National Laboratory, 9700 South Cass Avenue, Argonne, Illinois 60439, USA*
[2]*Materials Science Division, Argonne National Laboratory, 9700 South Cass Avenue, Argonne, Illinois 60439, USA*
[3]*Institute for Nonlinear Science, University of California at San Diego, 9500 Gilman Drive, La Jolla, California 92093, USA*
[4]*Division of Mathematical Sciences, National Science Foundation, 4201 Wilson Blvd., Arlington, Virginia 22230, USA*
(Received 13 December 2006; revised manuscript received 25 July 2007; published 6 November 2007)

This paper summarizes the results of numerical simulations of the interaction of a pair of biofilaments mediated by a molecular motor. The filaments are modeled as flexible rods, and the results are applicable to microtubules, which are relatively stiff, as well as to much softer filaments, such as actin. The results provide insight into the effects of flexibility on cytoskeleton formation and the rheology of semiflexible filament networks. The simulations are based on a nonlinear elasticity equation. The results show that flexibility enhances the tendency of filaments to align. The enhancement in turn favors the formation of large-scale structures in multifilament systems. Simulations for soft filaments show that the action of the motor can result in the formation of multiple loops of the filaments as a result of buckling, which can affect the structure of a cross-linked network and thereby its rheology. The estimate for the minimal buckling length as a function of the motor speed, the viscosity of the solvent, and the bending stiffness of the filament is derived analytically.

DOI: 10.1103/PhysRevE.76.051905 PACS number(s): 87.16.Ka, 87.16.Nn, 05.65.+b, 47.54.−r

I. INTRODUCTION

One of the primary functions of molecular motors is to form complex networks of long biofilaments (microtubules, actin, and others) and organize the cytoskeleton of the daughter cells during cell division [1]. *In vitro* experiments of the interaction of molecular motors and microtubules [2–7] performed in isolation from other biophysical processes that normally occur simultaneously *in vivo* have shown that, at sufficiently large concentrations of molecular motors and microtubules, the latter self-organize into starlike asters and rotating vortices, depending on the type and concentration of molecular motors.

This phenomenon of pattern formation in mixtures of microtubules and molecular motors can be studied in a multiscale framework. In Refs. [8,9] we developed a mesoscopic theory to explain the alignment of microtubules (see also Ref. [10]). The theory is based on a stochastic master equation that governs the evolution of the probability density of microtubules with a given orientation at a given location. The major assumption of the theory is that the complex process of interaction between microtubules and molecular motors can be approximated by simple binary inelastic collisions between rigid polar rods. The molecular motors enter into the theory in a certain probabilistic way: the probability of an interaction between microtubules is proportional to the local motor density. The inelasticity of collisions is manifested by the alignment of the rods after an interaction. For simplicity, binary interactions of microtubules are considered as instantaneous collisions that are mediated by uniformly distributed motors. The interaction between the rods on this level of description is addressed by a certain interaction kernel, localized in space, which depends on the position of the centers of mass of each rod and their mutual orientation. The stochastic master equation then gives rise to continuum or macroscopic coarse-grained equations. The main results obtained in Refs. [8,9] can be summarized as follows. (i) Spontaneous ordering transition to an oriented state occurs if the density of molecular motors exceeds some critical density. This critical density appears to depend on the degree of inelasticity of interaction between the rods. (ii) Ray-like objects (asters) and circular vortices appear as a result of the primary orientation instability in large enough systems. (iii) The transition between vortices and asters is controlled by the dwelling time of molecular motor at the end of microtubules, which is in turn represented in our theory by the corresponding anisotropy of the probabilistic interaction kernel.

In the mesoscopic theory [8,9], the details of the interaction kernel are assumed to be known and derived from simple micromechanical calculations with rigid rods. In the present paper we focus on such a micromechanical theory in detail. In particular, we are interested in quantifying the effects of flexibility of the filaments on the interaction kernel. Another nontrivial outcome of our studies is that in addition to alignment of stiff filaments, such as microtubules, molecular motors may produce a buckling instability in softer filaments such as actin.

Experiments [4–7] suggest the following qualitative picture of motor–filament interactions. If a free molecular motor binds to a microtubule at a random position, it marches along the filament in a fixed direction until it unbinds, perhaps after a period of dwelling at the end of the filament, as for NCD-type motors [11]. The position and orientation of the filament are essentially unchanged by the process, since the mass of the molecular motor is small in comparison with that of the microtubule. However, if a molecular motor binds to two microtubules (in experiments [4–7] the molecular motors form multiheaded constructs with more than two binding sites), it can change the relative position and orientation of the filaments significantly. Moreover, experiments performed with actin-myosin networks also indicate that myosin motors induce parallel alignment of actin filaments (dubbed zipping) [12]. Since most of the *in vitro* experiments with purified microtubules and motors are quasi-two-dimensional (i.e., the length of the microtubules typically exceeds the depth of the

 ©2007 The American Physical Society

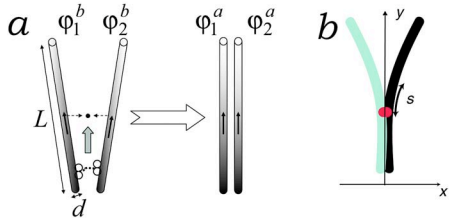

FIG. 1. (Color online) (a) A fully inelastic collision of two microtubules mediated by a molecular motor. (b) Schematic representation: The molecular motor is attached symmetrically to two flexible microtubules at a distance s along the tubule from the midpoint.

container), we consider the two-dimensional case only. While our technique can be also applied to the fully three-dimensional case with minor modifications, analysis of the potentially rich high-dimensional effects goes beyond the scope of this work.

A two-dimensional collision of two microtubules is schematically illustrated in Fig. 1(a). Before the interaction, the microtubules are oriented at angles φ_1^b and φ_2^b. The simultaneous binding of the molecular motor to the two microtubules and the subsequent marching along them results in a complete alignment of the latter; after the interaction the microtubules are oriented at angles φ_1^a and φ_2^a, where $\varphi_1^a=\varphi_2^a=\frac{1}{2}(\varphi_1^b+\varphi_2^b)$. We refer to this type of interaction as a fully inelastic collision, by analogy with the physics of inelastically colliding grains (see, for example, Ref. [13]). In Refs. [8,9] we showed that these inelastic collisions can lead to an orientational instability and a subsequent local ordering of filaments. The orientational instability can be compared to the clustering instability in dissipative granular gases [14]. Moreover, an inelastic collision is a reasonable and efficient characterization of the complicated filament zipping process occurring in the case of interaction between two soft filaments and multiple myosin motors (see Ref. [12]).

While a fully inelastic collision (perfect polar alignment) appears to be a simple and useful approximation, the details of the interaction of two microtubules mediated by a molecular motor are more complicated. A useful quantitative parameter that characterizes the inelasticity of the collision is the inelasticity factor

$$\epsilon = \varphi_f/\varphi_0, \tag{1}$$

where φ_f is the angle between the filaments after the interaction, $\varphi_f=|\varphi_1^a-\varphi_2^a|$, and φ_0 is the angle before the interaction, $\varphi_0=|\varphi_1^b-\varphi_2^b|$. Thus, $\epsilon=0$ for a fully inelastic collision ($\varphi_1^a=\varphi_2^a$) and $\epsilon=1$ for an elastic collision ($\varphi_f=\varphi_0$). The inelasticity factor characterizes the fraction of the initial angle that the rods recover after an interaction with a motor.

Our early micromechanical calculations [9] show that for pairs of rigid filaments the interaction mediated by a molecular motor is only partially inelastic and, in fact, the final angle $\varphi(s)$ depends on the position s of the initial attachment point on the tubule. A more meaningful concept is therefore the mean inelasticity factor

$$\bar{\epsilon} = \frac{\langle \varphi_f \rangle}{\varphi_0}. \tag{2}$$

Here the average is taken over all possible initial attachment positions; for filaments of length L, $-\frac{1}{2}L \leqslant s \leqslant \frac{1}{2}L$

$$\langle \varphi_f \rangle = L^{-1}\int_{-L/2}^{L/2} \varphi_f(s)ds. \tag{3}$$

Thus, $\bar{\epsilon}=0$ for fully inelastic interactions, $\bar{\epsilon}=1$ for fully elastic interactions.

The mean inelasticity factor $\bar{\epsilon}$ is a complicated nonlinear function of φ_0, but a good approximation for rigid filaments and small φ_0 is

$$\bar{\epsilon} \approx \frac{1}{2} + \frac{\operatorname{arcsinh}(\sqrt{\kappa}/2)}{\sqrt{\kappa(1+\kappa/4)}}. \tag{4}$$

Here κ measures the ratio of the translational and rotational viscous drag coefficients, $\kappa=(\xi_\parallel/\xi_r)L^2$ for tubules of length L. Numerically, κ is in the range of 12 to 15, so $\bar{\epsilon}\approx 0.63$ for rigid rods at small angles [9].

The sensitivity of the inelasticity factor to the initial attachment point is measured by the asymmetry coefficient $\bar{\alpha}$,

$$\bar{\alpha} = \frac{\langle s\varphi_f \rangle}{L\langle \varphi_f \rangle}. \tag{5}$$

For rigid rods, $\varphi_f(s)=\varphi_f(-s)$, so $\bar{\alpha}=0$. Note that the asymmetry coefficient differs from the collision kernel anisotropy introduced in Ref. [9]. The latter is related to the motor dwelling time at the end of microtubules; however, we anticipate that the effect of a strong asymmetry $\bar{\alpha}$ on pattern formation is similar to that of the kernel anisotropy; for example, it favors the formation of asters over vortices. Together, the two parameters $\bar{\epsilon}$ and $\bar{\alpha}$ quantify the collision kernel in the mesoscopic theory [9].

The purpose of this investigation is to study the mean inelasticity factor and asymmetry coefficients of interacting filaments with various degrees of flexibility. Using the continuum nonlinear elasticity equations, we show through numerical simulations that a finite bending flexibility amplifies the inelasticity of the collisions. In contrast, for much softer filaments, such as actin, molecular motors produce buckling instead of mutual alignment.

While microtubules are practically unbendable by thermal fluctuations (the thermal persistence length is of the order of a few mm, thus much larger than their contour length, which is a few tens of microns), molecular motors can bend them easily (see, e.g., Ref. [5]). Bending also increases the probability that two motors attach themselves simultaneously to two microtubules at different positions. When this situation occurs, the motors cross-link the microtubules, making them exactly parallel and thus realizing a fully inelastic collision $\bar{\epsilon}=0$ and the consequent zipping as observed in the experiments in Ref. [12]. Further simulations for more flexible biofilaments, such as actin, reveal a buckling instability and a formation of multiple loops. We were able to derive an analytic condition for the buckling instability and relate it to the motor speed, bending stiffness, and solvent viscosity. These

results provide insight into the effects of flexibility on cytoskeleton formation and the rheology of semiflexible filament networks.

Section II describes the details of the mathematical model underlying the numerical simulations. Section III summarizes the results of the numerical simulations for both microtubules and soft filaments. Section IV deals with the analytical consideration of the buckling condition. Section V contains our conclusions. Two Appendixes contain the technical details about the kinematics of filament interactions mediated by molecular motors (Appendix A) and the discretization of the mathematical model (Appendix B).

II. MODEL

Consider the interaction of two semiflexible rods (microtubules or, more generally, biofilaments) mediated by a molecular motor. We assume that the microtubules are of equal length L, where L is constant in time. That is, we focus on the case where the endpoints of the microtubules are stabilized, for example with taxol, so that the polymerization and depolymerization processes, which may affect the lengths of the microtubules, are insignificant. Furthermore, for simplicity we assume that the molecular motor attaches symmetrically to the microtubules. Thus, the two attachment points are at the same position on each rod with respect to their respective midpoints, and the force exerted by the motor is perpendicular to the bisector of the microtubule pair; see Fig. 1(b). The last conclusion follows from the assumption that the motor, while moving along the filaments with a constant speed, acts as a strong spring bringing the two motor heads together. In Appendix A we show that the motor has a tendency to orient perpendicular to the bisector of the microtubule pair even if the motor has a nonzero length. Since the initial attachment may occur at a random position on the tubule, we are interested in the properties of the interaction (in particular, the inelasticity coefficient) averaged with respect to the initial attachment position. We make the natural assumption that the probability of attachment is distributed uniformly along a microtubule. As mentioned above, we neglect the effects of thermal fluctuations on the microtubule shape. However, thermal fluctuations may have some effect on the shape of much softer biofilaments such as actin, whose thermal persistence length is of the order of a few microns. Moreover, we take the longitudinal and the transversal drag coefficients to be equal. This assumption is not significant and can be relaxed, although it does not affect the qualitative relation between filament flexibility and the inelasticity factor.

A. Kinematics

To describe the motion of interlinked microtubules, we combine the theory of Refs. [15,16] for a semiflexible polymer with the analysis of the rigid case in Ref. [9]. We adopt a two-dimensional setting and model a microtubule as a semiflexible homogeneous inextensible elastic rod of length L and bending stiffness β. We measure locations along the rod relative to the rod's midpoint, using the arclength s as the natural parameter, so $-\frac{1}{2}L \leq s \leq \frac{1}{2}L$ [see Fig. 1(b)]. The inextensibility of the rod implies that its embedding in the Euclidean plane preserves the arclength element at all times. Thus, if $\mathbf{r}(s)$ is the position in the plane of the point s on the tubule and $\mathbf{r}_s$ denotes its derivative with respect to s, then we have the local constraint $\mathbf{r}_s \cdot \mathbf{r}_s = 1$.

A molecular motor attaches initially to the tubule at the point s_i and moves along the tubule with the constant velocity v, exerting a force $\mathbf{f}$ on the tubule. As long as the force does not exceed a critical value, we may assume that the velocity of the motor does not depend on the force $\mathbf{f}$. However, we emphasize that this assumption is not essential; similar calculations can be carried out if the motor velocity depends on the force. Moreover, it can be rigorously shown that for rigid rods the particular velocity-force relation does not influence the value of inelasticity factor as long as the motors do not stall: the result for rigid filaments Eq. (4) does not depend on the motor velocity, the velocity-force relation affects only the interaction time. Qualitatively similar behavior is expected for semiflexible filaments, although the particular force-velocity relation may have some quantitative effect since the flexibility of the filaments introduces a new relaxation time scale. Since the velocity is fixed, the movement of the attachment point s_a is subject to the kinematic constraint

$$s_a(t) = s_i + vt. \tag{6}$$

In a binary collision, the molecular motor attaches to and moves along two microtubules simultaneously, and the relative configuration of the tubules changes as a result of the motor force acting on both tubules. As explained above, we consider only symmetric interactions, where the force is normal to the bisector. Then we can select a Cartesian coordinate system where the y-axis is directed along the bisector [see Fig. 1(b)], so $\mathbf{f} = (\pm f, 0)$, where the magnitude f of $\mathbf{f}$ has to be deduced from the kinematic constraint.

B. Governing equations

The equations governing the motion of the microtubules are derived from the balance of forces. If the viscosity of the medium containing the mixture is large (Stokes limit), then the viscous drag force is balanced by the force acting on the tubules. The latter is the variational derivative of the energy functional E measuring the bending energy of the tubule, together with the energy of the inextensibility and the motor attachment constraints

$$E = \frac{1}{2}\int_{-L/2}^{L/2} [g(\mathbf{r}_s \cdot \mathbf{r}_s - 1) + \beta \mathbf{r}_{ss} \cdot \mathbf{r}_{ss} + \mathbf{f} \cdot \mathbf{r}\,\delta(s - s_a)]ds. \tag{7}$$

Here, g is the line tension, which is determined implicitly from the length conservation constraint $|\mathbf{r}_s|^2 = 1$. The singular component of the energy is due to the kinematic constraint (6) and its form depends on the choice of the moving coordinate system that places the origin at the motor attachment point $\mathbf{r}(s_a)$. The equations of motion are found by taking variations

$$\eta\dot{\mathbf{r}} = -\frac{\delta E}{\delta \mathbf{r}} = \partial_s(g\mathbf{r}_s) - \beta\mathbf{r}_{ssss} - \frac{\mathbf{f}}{2}\delta[s - s_a(t)]$$

$$0 = -\frac{\delta E}{\delta g} = \mathbf{r}_s \cdot \mathbf{r}_s - 1, \quad 0 = -\frac{\delta E}{\delta f} = \mathbf{r}\delta[s - s_a(t)]. \tag{8}$$

Here, η is the viscous drag coefficient (per unit length). These equations can be interpreted as defining a gradient flow with respect to the variables $\mathbf{r}$, g, and $\mathbf{f}$, where the constraints are established instantaneously on the time scale of the viscous force.

The solution of Eqs. (8) must satisfy the integral relation

$$\int_{-L/2}^{L/2} (\eta\dot{\mathbf{r}} \cdot \delta\mathbf{r} + \delta E)ds = 0, \tag{9}$$

for all admissible variations $\delta\mathbf{r}$, δg and δf. The energy variation is

$$\delta E = \int_{-L/2}^{L/2} \left(g\mathbf{r}_s \cdot \delta\mathbf{r}_s + \beta\mathbf{r}_{ss} \cdot \delta\mathbf{r}_{ss} + \frac{1}{2}\delta(s - s_a)\mathbf{f} \cdot \delta\mathbf{r} \right) ds + \int_{-L/2}^{L/2} (\mathbf{r}_s \cdot \mathbf{r}_s - 1)\delta g ds + \int_{-L/2}^{L/2} \mathbf{r}\delta(s - s_a) \cdot \delta\mathbf{f} ds.$$

Taking Eq. (9) instead of Eq. (8) and demanding that it be satisfied for all admissible variations of $\mathbf{r}$, g, and $\mathbf{f}$, assumed independent, we obtain a weak form of the governing equations

$$\int_{-L/2}^{L/2} \left[\eta\dot{\mathbf{r}} \cdot \delta\mathbf{r} + g\mathbf{r}_s \cdot \delta\mathbf{r}_s + \beta\mathbf{r}_{ss} \cdot \delta\mathbf{r}_{ss} + \frac{\mathbf{f}}{2}\delta(s - s_a) \cdot \delta\mathbf{r} \right] ds = 0, \tag{10}$$

$$\int_{-L/2}^{L/2} (\mathbf{r}_s \cdot \mathbf{r}_s - 1)\delta g ds = 0, \quad \int_{-L/2}^{L/2} \delta(s - s_a)\mathbf{r} \cdot \delta\mathbf{f} ds = 0. \tag{11}$$

In this weak formulation there is no need for *a priori* assumptions on the smoothness of the solutions and their boundary conditions. If the solution is sufficiently smooth, however, we can integrate by parts and obtain the strong form of the governing equations

$$\int_{-L/2}^{L/2} \left[\eta\dot{\mathbf{r}} - \partial_s(g\mathbf{r}_s) + \beta\partial_s^4\mathbf{r} + \frac{1}{2}\delta(s - s_a)\mathbf{f} \right] \cdot \delta\mathbf{r} ds + [g\mathbf{r}_s \cdot \delta\mathbf{r} + \beta\mathbf{r}_{ss} \cdot \delta\mathbf{r}_s - \beta\mathbf{r}_{sss} \cdot \delta\mathbf{r}]_{-L/2}^{L/2} = 0.$$

The vanishing of the integral is equivalent to the equations of motion in the usual differential form (8), while the vanishing of the boundary term determines the natural boundary conditions

$$(g\mathbf{r}_s - \beta\mathbf{r}_{sss}) \cdot \delta\mathbf{r} + \beta\mathbf{r}_{ss} \cdot \delta\mathbf{r}_s + \frac{1}{2}\delta_{s_a,s_b}\mathbf{f} \cdot \delta\mathbf{r} = 0 \tag{12}$$

at each boundary point $s_b = \pm L/2$. The Kronecker delta symbol δ_{s_a,s_b} ensures the inclusion of the force in the boundary condition when the motor is attached at the boundary.

In the absence of smoothness assumptions, Eqs. (10), (11) implicitly contain the suitable weak version of the boundary conditions. In particular, the formulation (10), (11) does not change when $s_a = \pm L/2$, while for the equation above the term $\mathbf{f}$ becomes part of the boundary conditions.

The weak formulation is amenable to discretization in the presence of singular terms. One such term appears in the equation of motion for $\mathbf{r}$ as a result of the movable point force exerted by the motor. If an explicit equation of motion for the tension g is derived from the inextensibility constraint and the equations of motion for $\mathbf{r}$, an even more cumbersome singular term appears:

$$g_{ss} - \mathbf{r}_{ss} \cdot \mathbf{r}_{ss}g - \beta\mathbf{r}_s\partial_s^5\mathbf{r} + \frac{1}{2}\mathbf{r}_s\mathbf{f}\delta'(s - s_a) = 0. \tag{13}$$

This equation demands even higher regularity of $\mathbf{r}$ than the equation for $\mathbf{r}$ itself. We circumvent both problems by solving for the forces of the constraint g and $\mathbf{f}$ from the corresponding constraint equations, rather than deriving explicit equations for them. The result is a well-posed discrete problem that, however, requires an implicit time discretization (see Appendix B for details).

III. NUMERICAL EXPERIMENTS

Symmetric interactions of pairs of microtubules are simulated numerically by integrating the equations of motion (10), (11). In this section we present the results of two types of such simulations, first for (relatively stiff) microtubules and then for (fairly soft) actin filaments.

Physical parameters. The viscous drag coefficient per unit length η is related to the effective dynamic viscosity of the solvent μ; in a thin layer of solvent the approximate relation is $\eta \approx 2\pi\mu/\ln(\tilde{L}/d)$, where $\tilde{L}$ is a characteristic cut-off size of the problem (for example, the average filament length or the depth of the container), typically of the order 5 microns. This models the proximity of the container walls above and below the tubules (see also Refs. [5,17,18]). The bulk dynamic viscosity coefficient for water, the assumed solvent, is $\mu = 10^{-3}$ pN s μm^{-2}. Moreover, viscosity can increase significantly as a result of the presence of organic buffers, such glycerol etc., which are added to the solution. To account for these effects, we use the effective drag coefficient $\eta = \lambda\mu = \lambda \times 10^{-3}$ pN s/μm^2, where the factor λ was changed in our studies from $\lambda = 3$ to $\lambda = 15$ (for example, in simulations Ref. [5] was used $\lambda = 200$).

For microtubules we use the bending stiffness strength $\beta = 2.0 \times 10^{-23} Nm^2 = 20$ pN μm^2, as calculated in Ref. [17]. The motor velocity is set to $v = 1$ μm/s [5] and $\lambda = 3$ to account for the confinement in a thin layer. Note that by scaling space (hence the microtubule length) by a, the effective bending stiffness is scaled by a^{-4}, while the tension g and the force $\mathbf{f}$ (Lagrange multipliers) remain unchanged. Thus, we normalize space so that each tubule is of unit length. Time is normalized by using T, the length of time needed for the motor to traverse 1 μm ($T = 1$ s in our case), resulting in a nondimensional motor velocity $\hat{v} = vT/L$.

Effective bending stiffness. The introduction of an effec-

tive bending stiffness $\hat{\beta}=\beta L^{-4}\eta^{-1}T$ enables us to study the interactions of a range of tubules of different lengths by means of a single tubule of unit length but with different values for the effective bending stiffness and the motor velocity. Thus there is no need to change the spatial discretization of the microtubule to maintain accuracy. Moreover, as it follows from the expression for the effective bending stiffness $\hat{\beta}$, the main factor is the length which enters as L^4, whereas viscosity enters in only the first power. Thus, a small change in the filament length L can accommodate a considerable change in the solvent viscosity leaving the value of $\hat{\beta}$ unchanged.

Discretization parameters. In all simulations, we discretized the normalized tubule of length 1 with $\Delta s=0.03125$ or smaller, and time with $\Delta t=0.01$. Simulations of tubules of different lengths ($L=15,30,45,60$ μm) were accomplished by adjusting the effective bending stiffness, as explained in the previous paragraph: $\hat{\beta}=1.32\times10^{-1}$, $8.23\times10^{-3}, 1.63\times10^{-3}, 5.14\times10^{-4}$; the effective drag coefficient, $\hat{\eta}=1.0$; the effective motor velocity, $\hat{v}=0.067,0.033,0.022,0.017$.

After the interaction, the tubule is allowed to relax until the filament assumes an almost straight configuration; that is, the mean relative deviation of the tangent from the mean is less than 10^{-2}. This process was carried out in two different ways, with the motor sliding off the tubule and with the motor dwelling at the end of the tubule, until the relaxation is complete. The dwelling was introduced to model different types of motors. It is known that some motors, such as kinesin, have almost zero dwelling time, whereas the NCD-type motor complexes used in experimental works (see Refs. [4,5]) appear to have a very large dwelling time at the microtubule ends.

A. Bending of microtubules

Figure 2 shows two typical examples of the time evolution of the interaction of a pair of relatively stiff microtubules mediated by a molecular motor. In both cases, the motor induces a significant deformation of the filament shape. The tubules curve in such a way that the segments of microtubules behind the moving motor become locally more aligned than if the tubules were straight. This curvature increases the probability of attachment of additional motors and, therefore, the probability of cross-linking of the tubules in several places. Multiple cross-linking is expected to quickly align the two tubules; however, a consideration of the action of multiple motors is beyond the scope of the present work.

Figure 3 shows the evolution of the filament tension $g(s)$ in the course of the interaction. The filaments become stretched ($g>0$) ahead of the motor attachment point ($s>s_a$) and slightly compressed ($g<0$) behind the attachment point ($s<s_a$). In the limit of zero motor size, the tension exhibits a discontinuity at the attachment point ($s=s_a$) because of the δ-function character of the motor force $\mathbf{f}$. In our numerical procedure this discontinuity is regularized as a result of the weak formulation. The negative tension g is a precursor of the Euler buckling instability for elastic rods [20]. However, buckling of microtubules does not occur because of the large value of the stiffness coefficient β (see Sec. IV).

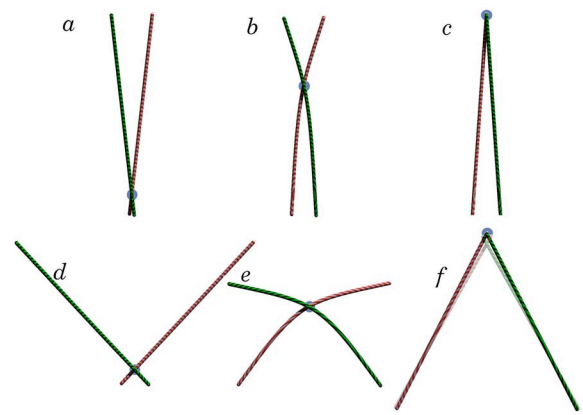

FIG. 2. (Color online) Two sequences of images illustrating the bending and alignment of microtubules by molecular motors, with dwelling of the motor at the end of the microtubules. (a)–(c) Initial angle $\varphi_0=14°$, (d)–(f) initial angle $\varphi_0=90°$. The shaded region indicates the motor location; the motor moves upward. For comparison, the image (f) also shows the configuration of the two microtubules if the dwelling time is zero (shown by semitransparent colors). The sequence shows the configurations at times $t=3$ (a), (d), $t=33$ (b), (e), and $t=180$ (c), (f) for $\beta=20$ pN μm^2, $L=60$ μm, motor velocity $v=1$ μm/s. The viscosity equals $3\times$ viscosity of water ($\lambda=3$) with initial attachment offset 6 μm from the tubule end. After the interaction with the motor, the initial angle is reduced from 14° to 8.7° with dwelling and from 90° to 58.3° with dwelling and to 62.2° without dwelling (shaded). More detailed images can be found in Ref. [19], movies 1–3.

Figures 4–7 show the results for the inelasticity factor $\bar{\epsilon}$ and asymmetry coefficient $\bar{\alpha}$. There is an overall tendency for $\bar{\epsilon}$ to decrease with the length L of the tubule (and, there-

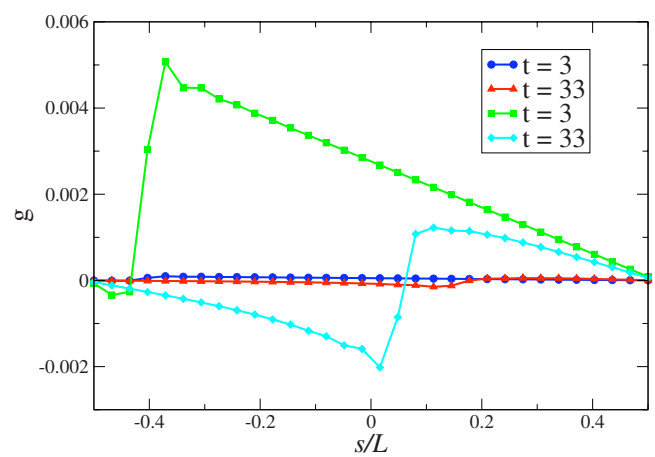

FIG. 3. (Color online) Tension in the tubule configurations of Fig. 2 at times $t=3$ (a),(d) and $t=33$ (b),(e); $\beta=20$ pN μm^2, $L=60$ μm, $v=1$ μm/s, and $\lambda=3$. At the final stages (e), (f), the tension is zero (not shown). The tension g changes sign and varies very rapidly near the motor attachment point. A smaller initial angle ($\varphi_0=14°$) results in a tension approximately 10 times smaller than that of the larger initial angle (90°).

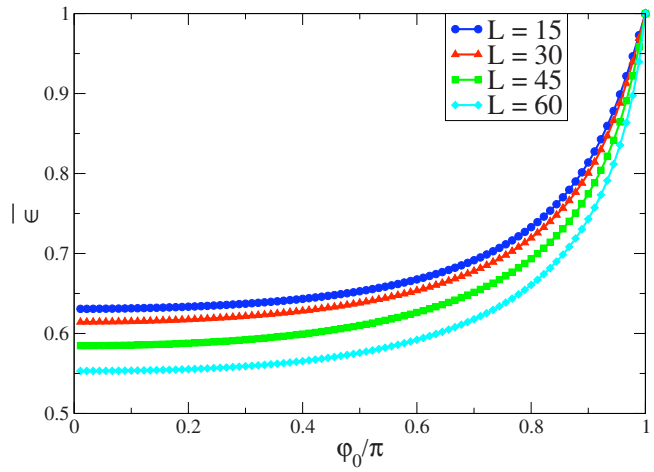

FIG. 4. (Color online) Inelasticity factor $\bar{\epsilon}$ with dwelling, for different lengths of microtubules; β=20 pN μm^2 and λ=3.

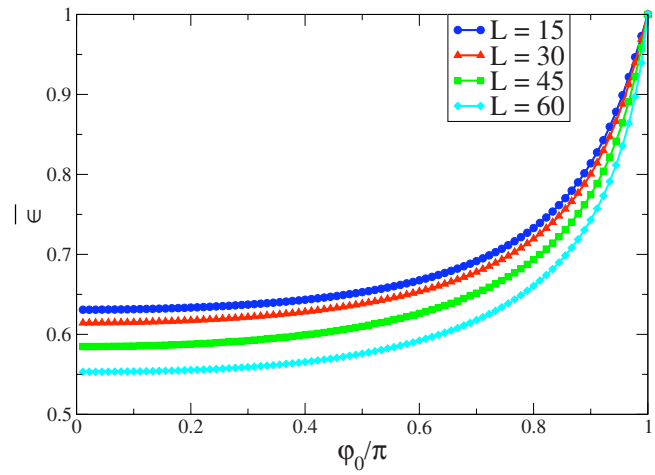

FIG. 6. (Color online) Inelasticity factor $\bar{\epsilon}$ without dwelling as a function of the tubule length; β=20 pN μm^2 and λ=3.

fore, to increase with the bending stiffness β, since in the rescaled variables β is proportional to L^{-4}). As $\beta \to \infty$, $\bar{\epsilon}$ approaches the stiff limit value 0.63; see Eq. (4).

In contrast, the dwelling of the motors at the tubule ends has a relatively small effect on the inelasticity if the tubules are sufficiently stiff, although it may affect other properties of the interaction, such as the anisotropy of the kernel [9]. As one sees from Figs. 4–6, the inelasticity factor $\bar{\epsilon} \to 1$ for $\varphi_0 \to \pi$; that is, almost antiparallel filaments do not change their mutual orientation after an interaction with motors. This trend is similar to that of rigid filaments [9].

A decrease in the stiffness induces a significant asymmetry of the inelasticity with respect to the location of the initial attachment point s_i, as measured by the asymmetry coefficient $\bar{\alpha}$. However, our calculations show that $\bar{\alpha}$ remains relatively small for typical filament lengths used in the majority of experiments ($\bar{\alpha} < 0.03$). This result suggests that the kernel anisotropy related to dwelling of the motors [9] rather than the asymmetry coefficient is the dominant factor affecting the large-scale pattern selection, such as transitions between vortices and asters.

The dependence of the mean inelasticity $\bar{\epsilon}$ and its asymmetry $\bar{\alpha}$ on the tubule length and, hence, the effective stiffness are illustrated in Figs. 8 and 9. For the dwelling case, there is an overall trend of decreasing the inelasticity factor $\bar{\epsilon}$ with the increase of the length. For very large rod lengths, $\bar{\epsilon}$ approaches the value 0.42, which is significantly lower than the value for rigid rods 0.63. Thus, our results indicate that the interaction becomes more inelastic with the increase of the length of filaments (equivalently, with the decrease of stiffness). Even for very long filaments, however, the interaction is not fully inelastic. This is because a single motor cannot align the filaments completely. However, multiple motors, cross-linking filaments in various locations, will rapidly make filaments parallel (zipping). Surprisingly, the dependencies are not monotonic for the no-dwelling case. This observation is likely related to the buckling of the rods when the filament length exceeds a certain critical value (see below).

B. Bending of actin filaments

The same modeling approach can be applied to much softer filaments, such as actin, interacting, for example, with myosin motors. According to Ref. [6], as with kinesin and

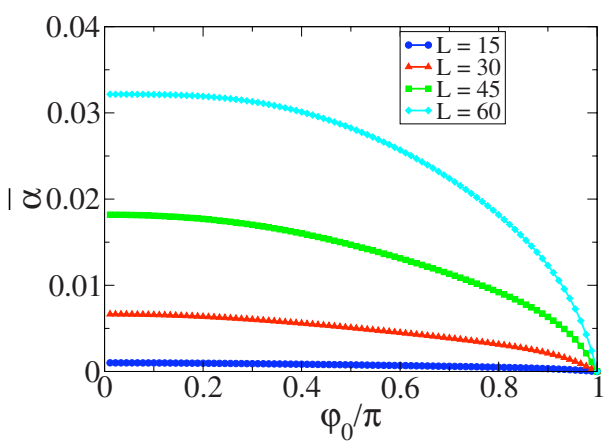

FIG. 5. (Color online) Asymmetry coefficient $\bar{\alpha}$ with dwelling, for different lengths of microtubules; β=20 pN μm^2 and λ=3.

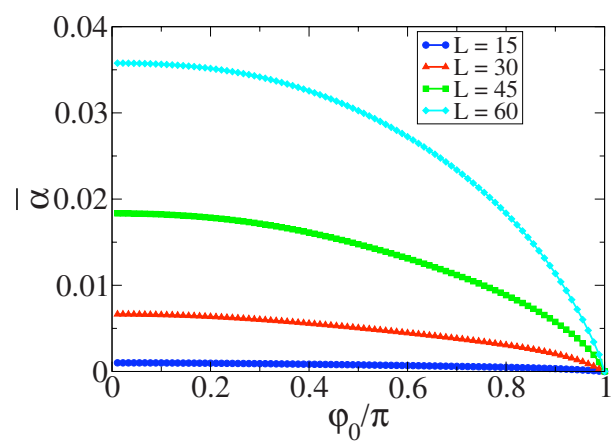

FIG. 7. (Color online) Asymmetry coefficient $\bar{\alpha}$ without dwelling as a function of the tubule length; β=20 pN μm^2 and λ=3.

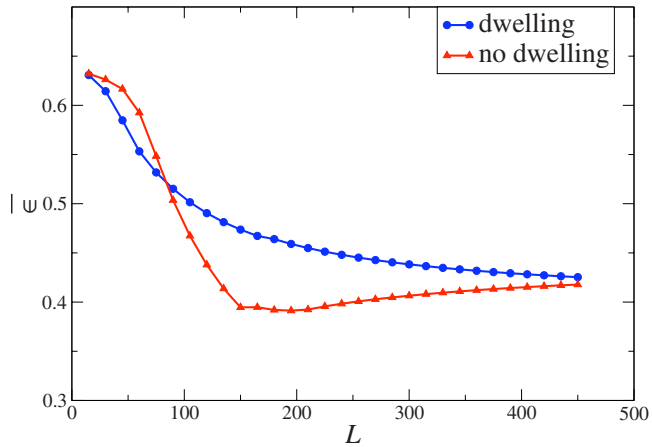

FIG. 8. (Color online) Inelasticity factor for $\varphi_0=4°$ as a function of the tubule length (and, by implication, as a function of the effective bending stiffness of a unit tubule); $\beta=20$ pN μm^2 and $\lambda=3$.

NCD considered in the previous section, myosin motors also form multiheaded complexes. The main difference is that the stiffness of actin is about 10^3 times smaller than that of microtubules ($\beta=7.3\times10^{-2}$ pN μm^2). We studied actin filaments of length $L=50$ μm in a solvent with $\lambda=3$ and $\lambda=15$, the latter being equivalent to a system of filaments of length $L\approx26$ in a solvent with $\lambda=200$.

Our simulations with $\lambda=15$ produced a surprising result: the interaction of the motor with two actin filaments result in the creation of complex multilooped structures, as shown in Fig. 10. These loops are the result of Euler bending instability of elastic rods. Experiments with a lower viscosity $\lambda=3$ do not produce buckling, suggesting that there is a critical value of η or, equivalently, of length L, above which buckling appears (see the following section). As loops form, tension g becomes negative and exhibits oscillations (see Fig. 11). After the motor reaches the end of the filaments, buckling slowly relaxes because of the finite bending rigidity.

The evolution of the root mean square tension $\bar{g}=L^{-1}\sqrt{\int_0^L g(s)^2 ds}$ as a function of time is shown in Fig. 12 for

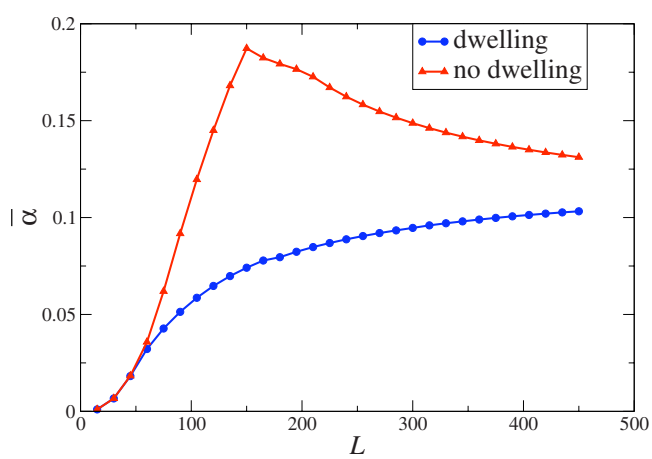

FIG. 9. (Color online) Asymmetry coefficient $\bar{\alpha}$ for $\varphi_0=4°$ as a function of tubule length (and, by implication, as a function of the effective bending stiffness of a unit tubule); $\beta=20$ pN μm^2 and $\lambda=3$.

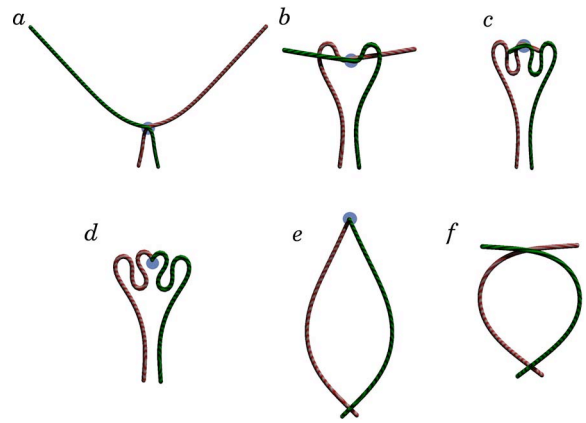

FIG. 10. (Color online) Two sequences of images illustrating the bending and alignment of actin-like filaments by molecular motors: (a)-(d) with motor in motion, (e) with motor dwelling at the end of the filaments after interaction, and (f) filaments freely relaxing after interaction. The shaded region indicates the motor location; the motor moves upward. Images are shown at times $t=1.5$ (a), $t=9$ (b), $t=12.5$ (c) $t=13.5$ (d), and $t=100.0$ (e),(f); $\beta=7.3\times10^{-2}$ pN μm^2, $L=50$ μm, $v=1$ μm/s, and $\lambda=15$. The images (e) and (f) illustrate the difference between dwelling and nondwelling interactions. In both cases, the initial angle is $\varphi_0=90°$, and the initial attachment offset is 1 μm from the end of the filament. After the interaction with the motor, the initial angle is reduced to 19.9° with dwelling and to 32.7° without dwelling. More detailed images can be found in Ref. [19], movies 3 and 4.

both $\lambda=3$ and 15. As one sees, the asymptotic decay of $\bar{g}$ is exponential, with the exponent determined mostly by the viscosity of the solvent (characterized relative to the viscosity of water by the constant λ). Dwelling also affects the decay rate. For intermediate times, however, the behavior is different, consistent with some power-law (see the inset to Fig. 12). According to Ref. [21], for a buckled filament confined between two rigid walls, the tension exhibits a power-law

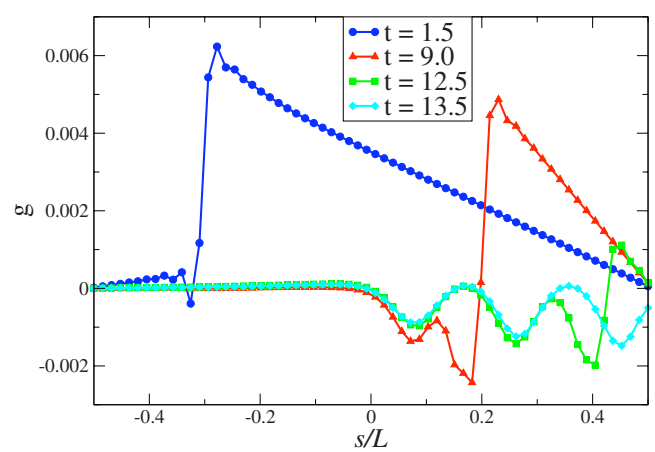

FIG. 11. (Color online) Tension in the actin configurations of Fig. 10 at times (a) $t=1.5$; (b) $t=9$; (c) $t=12.5$; (d) $t=13.5$; $\beta=7.3\times10^{-2}$ pN μm^2, $L=50$ μm, $v=1$ μm/s, and $\lambda=15$. With the motor attached near the very end ($t=13.5$), the tension has an oscillatory profile that decays rapidly to an essentially tension free profile ($g\approx0$, not shown), regardless of whether the motor is still attached (dwelling) or not (without dwelling).

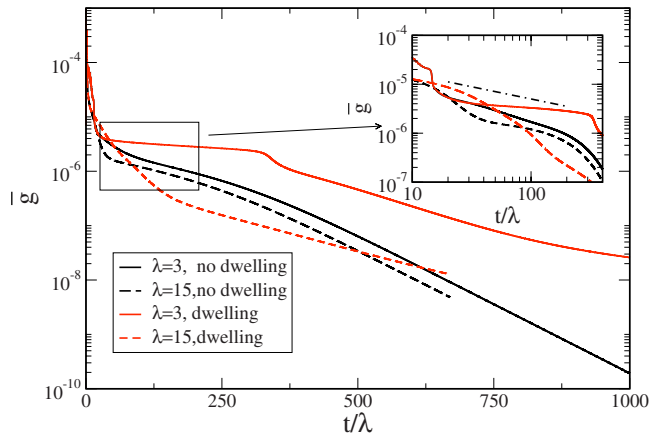

FIG. 12. (Color online) Evolution of mean root square tension $\bar{g}$ for $L=50$ with two different values of the solvent viscosity $\lambda=3$ and $\lambda=15$. The plots are shown in semilogarithmic scale. Black curves depict $\bar{g}$ for the case of filaments without dwelling, and red lines with dwelling. The inset shows a blow-up of the region in the box on the main plot, in log-log scale. The dot-dashed line displays the power law $\bar{g}\sim 1/\sqrt{t}$.

relaxation depending on the initial deformation, whereas slightly bent filaments relax as $\bar{g}\sim 1/\sqrt{t}$. Thus, in our situation, the relaxation dynamics is rather different.

Moreover, dwelling can have a significant effect on the inelasticity factor because of the very slow straightening of the filaments (see Fig. 10). The difference stems from the fact that in contrast to rigid rods, soft filaments possess an additional time scale $\sim 1/\hat{\beta}$ related to the straightening of the rod. Since actin-like filaments are strongly bent when the motor reaches the end-point position, further relaxation dynamics is very sensitive to whether the motor leaves the filaments or binds their ends together.

The complex structures shown in Fig. 10 may appear in the course of cytoskeleton formation and should affect the rheological properties of the filament networks. Since actin filaments take significantly longer to relax back to the unbent configuration, the notion of an inelastic collision, which was introduced for stiff microtubules, is essentially inapplicable to actin. The formation of loops in actin filaments should facilitate multiple motor bindings and thus the creation of bundles. The dynamics of actin filaments and active filament networks will be examined in more detail in a forthcoming publication.

IV. BUCKLING CONDITION

To understand the buckling instability of straight semiflexible filaments driven by molecular motors, we consider the situation when the filaments are exactly anti-parallel (i.e., $\varphi_0=\pi$). For this configuration the tension $g(s,t)$ and the buckling threshold can be found analytically. We believe that the calculations for the antiparallel configuration capture the most important aspects of the buckling instability, whereas the derivation of the buckling criterion for arbitrary initial angles φ is greatly complicated by the rotation and bending of the filaments.

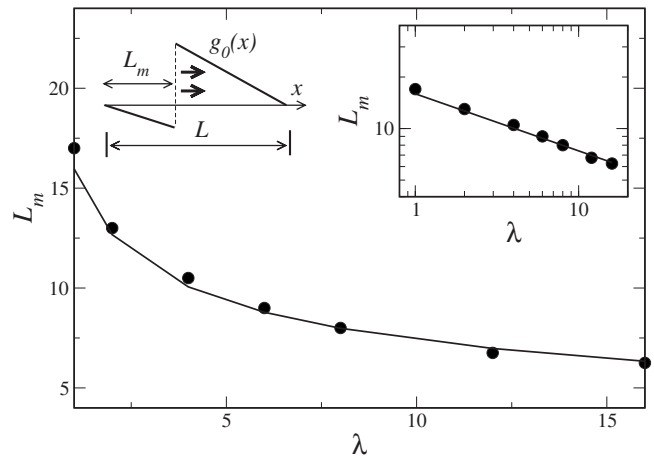

FIG. 13. The dependence of the length behind motor attachment at the onset of buckling L_m (in microns) on the normalized solvent viscosity $\lambda=\eta/\eta_0$, where η_0 is the viscosity of water. Symbols show results of numerical solution of Eq. (8) for $\phi_0=\pi$ and $L=50$ μm, $\beta=7.3\times 10^{-2}$ pN μm^2 (actin). The solid line shows solution to Eq. (20), no fitting parameters. The right inset shows L_m vs λ on a log-log scale. The left inset illustrates the tension distribution g_0 for a single filament of an antiparallel pair; the motor moves to the right, pushing the filament to the left; tension g_0 is piecewise linear, vanishes at the ends, with a discontinuity at the motor attachment point.

We choose filament orientation along the x axis [i.e., $\mathbf{r}=(s,0)$]. The motion of the filament is opposite to the motion of the motor, which moves with the speed v in the positive x direction (see the left inset in Fig. 13). Taking this into account, Eq. (8) yields

$$-v\eta=\partial_x g_0-\frac{f}{2}\delta[x-s_a(t)], \tag{14}$$

which is an equation for the tension g_0.

The tension distribution following from Eq. (14) satisfying boundary conditions $g_0=0$ at the ends of filament $s=x=\pm L/2$ is of the form

$$g_0(s,t)=\begin{cases}-v\eta(x+L/2) & \text{for } x<s_a(t),\\ -v\eta(x-L/2) & \text{for } x\geq s_a(t).\end{cases} \tag{15}$$

As one sees from Eq. (15) (schematically illustrated in the left inset to Fig. 13), behind (or to the left of) the motor attachment point the tension $g=g_0(x,t)$ is negative because that segment is being compressed (or pushed); on the segment ahead (to the right) of the motor the tension is positive since the segment is being stressed (or pulled). At the motor attachment point $x=s_a$ the tension g_0 is discontinuous; the value of the motor force f can be obtained from the jump of the tension. This analytic expression is consistent with tension distributions found numerically (see Fig. 3).

Negative tension behind the motor is a precursor of buckling. However, due to a nonuniform tension distribution the buckling condition is different from the classical Euler buckling and the buckling of semiflexible filaments studied in Refs. [22,23] in the context of microtubules' buckling, which was induced by a compressive force F_0 applied at the end

and with lateral confinement. Consequently, our analysis is more complicated.

To examine the buckling instability we consider a small perturbation $\xi=(\xi_x,\xi_y)$ about a straight horizontal filament: $\mathbf{r}=\mathbf{x}_0 s+\boldsymbol{\xi}$, where $\mathbf{x}_0$ is the unit vector in the x direction. After a linearization of Eq. (8), we derive the following equation for the transverse perturbation ξ_y (it is easy to see that the parallel perturbation ξ_x plays no role in the linear order):

$$\eta\partial_t\xi_y = \partial_x[g_0(x,t)\partial_x\xi_y] - \beta\partial_x^4\xi_y, \tag{16}$$

with the boundary conditions $\partial_x^2\xi_y=0$ at $x=\pm L/2$.

Equation (16) is still a formidable problem because of the explicit time dependence of tension $g_0(t)$ due to the motor motion, $s_a(t)=s_i+vt$ [see Eq. (6)]. Further simplification is possible by assuming that the buckling instability happens faster then the time scale associated with motion of the motor L/v, which is true for sufficiently long filaments. In this situation one can study the linear problem (16) with a "frozen" tension (i.e., s_a=const); the time dependence of the perturbation ξ_y is then described by $\xi_y\sim\exp(\sigma t)$, where σ is the growth rate.

The instability (and therefore buckling) occurs when the maximum value of the growth-rate σ crosses zero. The profile of this critical mode can be obtained from the stationary equation (16), so that the onset of the instability is signaled by the appearance of a nontrivial solution of the following equation:

$$\partial_x(g_0(x,t)\partial_x\xi_y) - \beta\partial_x^4\xi_y = 0. \tag{17}$$

The existence of nontrivial solutions to this equation, and hence the instability threshold, is determined in terms of the model parameters: the length of filament L, motor velocity v, viscosity η and bending stiffness β. Equation (17) can be rewritten as a second-order boundary value problem by substituting $W=\partial_x\xi_y$, integrating once along the x direction, and using the boundary condition $g_0\partial_x\xi_y-\beta\partial_x^3\xi_y=0$ at $x=s=\pm L/2$, as implied by Eq. (12). This kills the constant of integration and yields equation

$$g_0(x,t)W - \beta W_{xx} = 0 \tag{18}$$

with the boundary conditions $W_x=0$ at $x=\pm L/2$, and g_0 given by Eq. (15). The solution of Eq. (18) depends on the motor attachment position s_a; since g_0 is discontinuous at this point, we only demand the continuity of W and W_x at $x=s_a$.

Nontrivial solutions of Eq. (18) with the imposed boundary conditions do not exist for arbitrary values of the filament length L. In fact, for fixed v,η,β there is a certain critical value L^* so that no nontrivial solutions exist if $L<L^*$ and a solution appears for $L=L^*$ and $s_a=L/2$. Furthermore, for each filament length $L>L^*$ one can find the attachment position s_a corresponding to the onset of buckling. Correspondingly, the length $L_m=s_a+L/2$ is the minimal size of the compressed segment of the filament to the left of the motor that can buckle; thus, $L_m\leq L^*$, see Fig. 13.

It is useful to consider L_m in the limiting case of a very long filaments ($L\to\infty$). In this case we can consider Eq. (18) on the left segment of length L with the boundary condition $W=0$ at the right end of the segment, i.e., at $x=s_a$. To see this, note that ahead of the motor attachment point tension $g_0=v\eta(L/2-s_a)>0$ is positive (the filament is being pulled), vanishes at the right end, and if $L-L_m\gg 1$ the corresponding Airy functions and their derivatives decay very fast away from the right end of the filament (the corrections for the finite size of $L-L_m$ are small). Therefore, for $L\to\infty$ the continuity condition for functions $W,\partial_x W$ at $x=s_a$ can be replaced by the asymptotic values to the right of s_a: $W(x=s_a)=0$. Making the substitution $x\to x+L/2$, Eq. (18) gives rise to the Airy equation

$$v\eta x W + \beta W_{xx} = 0 \tag{19}$$

with the boundary conditions $W_x=0$ at $x=0$ and $W=0$ at $x=L_m$. Applying the solvability criterion to this reduced system, we find that nontrivial solutions corresponding a buckling deformation (i.e., nonmonotone solutions) to Eq. (19) appear when the following condition is satisfied:

$$L_m \approx 3.82\left(\frac{\beta}{v\eta}\right)^{1/3}. \tag{20}$$

Expression (20) for the length L_m is notably different from the classical Euler buckling condition due to a compressive force F at the boundary, which gives $L_{\text{Euler}}\sim\sqrt{\beta/F}$ [24].

For the parameters of our numerical experiments $v=1\ \mu\text{m/s}$ and $\eta\approx 0.015\ \text{pN s}/\mu\text{m}^2$ (about 15 viscosity of water), we obtained that the critical length $L_m\approx 60-70\ \mu\text{m}$ for microtubules and $L_m\approx 5-6\ \mu\text{m}$ for actin. Thus, it indicates that microtubules will not buckle under the action of an individual motor (a microtubule's length is typically 10–20 micron), which is fully consistent with our simulations. In contrast, dilute solution of sufficiently long actin filaments can buckle easily. However, the buckling can be suppressed in dense networks of interconnected actin filaments (in realistic actin networks the mesh size could be as small as 1–2 microns).

We have computed L_m numerically for the case of actin parameters with different values of the normalized viscosity λ. The resulting L_m as a function of λ is shown in Fig. 13. Overall, there is an excellent agreement with the theoretical prediction of Eq. (20). Moreover, the dependence of L_m on λ exhibits a powerlaw behavior with the exponent $-1/3$, as predicted by the theory (see the right inset to Fig. 13).

V. CONCLUSIONS

In this paper we have investigated the interaction of a pair of biofilaments (microtubules, actin filaments) mediated by a molecular motor. Our main result is that bending effects amplify the tendency of microtubules to align and, consequently, to form structures with large-scale ordering, such as asters and vortices. Our results support the observations made in Refs. [4,5] that bending effects are important for the explanation of self-organization processes in molecular motor-microtubule mixtures where bent microtubules were indeed observed. However, our calculations show that the flexibility alone cannot explain complete alignment of filaments (zipping) by a single molecular motor. It suggests that

action of multiple motors (and possibly static crosslinkers) is important to explain pattern formation in Refs. [4,5]. Moreover, recent experiments with actin-myosin gels indicate that indeed static crosslinkers acting along with dynamic motors greatly enhance the tendency towards pattern (bundle) formation, likely due to stronger alignment interactions [25]. Thus, our studies provide a quantitative characterization of the complicated filament-motor interaction processes, possibly shedding additional light onto the experimentally observed zipping phenomenon in actin-myosin systems [12].

Our studies indicate that molecular motors have a very strong and nontrivial effect on the shape of much softer filaments such as actin, resulting in Euler-type buckling instabilities and the formation of multiloop structures. Our analysis indicates that the buckling is strongly enhanced by increasing the viscosity of the solvent. The minimal length of the filament exhibiting buckling under the action of a motor is obtained analytically. While our result is derived for the antiparallel configuration, we anticipate that the estimate for the minimal buckling length L_m, Eq. (20), will be applicable, essentially unchanged, even for the initial angles $\varphi_0 \neq \pi$. As follows from our simulations of actin-type filaments depicted in Fig. 10, prior to buckling soft filaments become practically antiparallel ahead of the motor attachment point, while becoming nearly straight and parallel behind the motor (zipping) [see Figs. 10(a) and 10(b)]. Presumably, buckling effects have a strong influence on the rheological properties of interconnected (but rather dilute) actin networks interacting with myosin motors.

ACKNOWLEDGMENTS

The authors thank Jacques Prost, Francois Nédélec, Frank Jülicher, Karsten Kruse, and Erwin Frey for useful discussions. This work was supported by the U.S. Department of Energy, Grants No. DE-AC02-06CH11357 (D.K., H.G.K., I.A.) and No. DE-FG02-04ER46135 (L.T.).

APPENDIX A: SYMMETRIC ATTACHMENT LIMIT

In this Appendix we show that the tendency for a pair of stiff filaments (microtubules) to orient themselves perpendicularly to their bisector persists even in the case of nonzero length motors. The filaments are assumed to be of the same length, with the motor attached at an equal distance from the minus end of each filament (even attachment) and oriented transversally to the bisector of the filament pair (symmetric attachment). The general idea of symmetrization of motor attachment is captured in the case of rigid tubules connected by a stiff (but flexible) motor of length h, where $h \ll L$. The motion then reduces to a system of ordinary differential equations governing the overdamped motion of a system of two rigid rods (microtubules) connected by flexible inextensible link of the length h (motor) as depicted in Fig. 14.

In a fixed coordinate system the centers of mass of the tubules are at $\mathbf{c}^{(1)}$ and $\mathbf{c}^{(2)}$, respectively, while the motor attachment points are at $\mathbf{c}^{(1)}+\mathbf{t}^{(1)}$ and $\mathbf{c}^{(2)}+\mathbf{t}^{(2)}$. In terms of the distances from the respective centers $s_{1,2}$ we have $\mathbf{t}^{(1,2)} = s_{1,2}\hat{\mathbf{t}}^{(1,2)}$. The motor is represented by the vector $\boldsymbol{\tau}$; $\mathbf{n}^{(1)}$, $\mathbf{n}^{(2)}$,

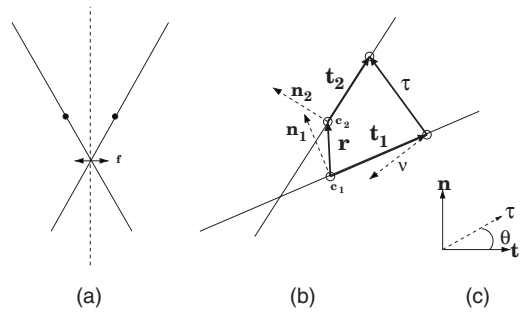

FIG. 14. Initial state of a symmetric microtubule pair: force acts on the microtubules perpendicular to the bisector; (a) attachment point is equidistant from the centers of mass; (b) inflexible tubules connected by a finite-size motor; (c) a vector in an orthonormal frame.

and $\boldsymbol{\nu}$ are normal to $\mathbf{t}^{(1)}$, $\mathbf{t}^{(2)}$, and $\boldsymbol{\tau}$, respectively; and hats denote unit vectors.

The dynamics of the system are determined as in the semiflexible case by the balance of forces and the kinematic constraint $\frac{d}{dt}s_{1,2}=v$,

$$\frac{d}{dt}\mathbf{c}^{(1,2)} = \pm f[\xi_{\parallel}^{-1}(\hat{\mathbf{t}}^{(1,2)},\hat{\boldsymbol{\tau}})\hat{\mathbf{t}}^{(1,2)} + \xi_{\perp}^{-1}(\hat{\mathbf{n}}^{(1,2)},\hat{\boldsymbol{\tau}})\hat{\mathbf{n}}^{(1,2)}],$$

$$\frac{d}{dt}\mathbf{t}^{(1,2)} = v\hat{\mathbf{t}}^{(1,2)} \pm f\xi_r^{-1}s_{1,2}{}^2[\hat{\mathbf{t}}^{(1,2)},\hat{\boldsymbol{\tau}}]\hat{\mathbf{n}}^{(1,2)}, \tag{A1}$$

where $\xi_{\parallel}^{-1}$, $\xi_{\perp}^{-1}$, and ξ_r^{-1} denote the inverses of tangential, transversal, and rotational viscosities; the motor force of magnitude f is directed along $\hat{\boldsymbol{\tau}}$, the sign depending on the direction from the tubule.

To obtain the force f and the motor motion, we observe the geometric constraint $\boldsymbol{\tau}=(\mathbf{c}^{(2)}-\mathbf{c}^{(1)})+(\mathbf{t}^{(2)}-\mathbf{t}^{(1)})$ (Fig. 14). Since the motor is rigid, its velocity must be directed along the normal $\hat{\boldsymbol{\nu}}$. Since the motor is rigid, its velocity is directed along the normal: $\dot{\boldsymbol{\tau}}=h\dot{\theta}\hat{\boldsymbol{\nu}}$. Here $\dot{\theta}$ denotes the angular velocity, which is independent of the choice of an orthonormal coordinate system. We obtain the relations

$$\begin{aligned} h\dot{\theta}\hat{\boldsymbol{\nu}} = &-f\xi_{\parallel}^{-1}[(\hat{\mathbf{t}}^{(1)},\hat{\boldsymbol{\tau}})\hat{\mathbf{t}}^{(1)} + (\hat{\mathbf{t}}^{(2)},\hat{\boldsymbol{\tau}})\hat{\mathbf{t}}^{(2)}] - f\xi_{\perp}^{-1}[(\hat{\mathbf{n}}^{(1)},\hat{\boldsymbol{\tau}})\hat{\mathbf{n}}^{(1)} \\ &+ (\hat{\mathbf{n}}^{(2)},\hat{\boldsymbol{\tau}})\hat{\mathbf{n}}^{(2)}] + v(\hat{\mathbf{t}}^{(2)} - \hat{\mathbf{t}}^{(1)}) - f\xi_r^{-1}(s_1^2[\hat{\mathbf{t}}^{(1)},\hat{\boldsymbol{\tau}}]\hat{\mathbf{n}}^{(1)} \\ &+ s_2^2[\hat{\mathbf{t}}^{(2)},\hat{\boldsymbol{\tau}}]\hat{\mathbf{n}}^{(2)}). \end{aligned} \tag{A2}$$

Denote by $\mathbf{v}_{\hat{\mathbf{u}}}=(\mathbf{v},\hat{\mathbf{u}})\hat{\mathbf{u}}$ the component of a vector $\mathbf{v}$ along the unit vector $\hat{\mathbf{u}}$. Projecting the constraint (A2) onto the motor furnishes an equation for f independent of the motor size [26],

$$\begin{aligned} 0 = f[&\xi_{\parallel}^{-1}(|\hat{\boldsymbol{\tau}}_{\hat{\mathbf{t}}^{(1)}}|^2 + |\hat{\boldsymbol{\tau}}_{\hat{\mathbf{t}}^{(2)}}|^2) + \xi_{\perp}^{-1}(|\hat{\boldsymbol{\tau}}_{\hat{\mathbf{n}}^{(1)}}|^2 + |\hat{\boldsymbol{\tau}}_{\hat{\mathbf{n}}^{(2)}}|^2) \\ &+ \xi_r^{-1}(s_1^2|\hat{\boldsymbol{\tau}}_{\hat{\mathbf{n}}^{(1)}}|^2 + s_2^2|\hat{\boldsymbol{\tau}}_{\hat{\mathbf{n}}^{(2)}}|^2)] + v(\hat{\mathbf{t}}^{(2)} - \hat{\mathbf{t}}^{(1)},\hat{\boldsymbol{\tau}}). \end{aligned}$$

The coefficient of f vanishes only if $\boldsymbol{\tau}$ is normal to both tangential and both normal vectors of the tubules, a condition that is clearly impossible even in the case of alignment. Hence, the force f is uniquely determined from the above relation and is $O(1)$ relative to the motor size.

To determine the relative position of the motor and the tubules, we project the constraint (A2) onto $\hat{\mathbf{t}}^{(1)}+\hat{\mathbf{t}}^{(2)}$, which is along the tubule bisector. This eliminates the term with v (a rhombus has orthogonal diagonals),

$$f^{-1}h\dot{\theta}(\hat{\boldsymbol{\nu}},\hat{\mathbf{t}}^{(2)}+\hat{\mathbf{t}}^{(1)}) = \xi_{\parallel}^{-1}[1+(\hat{\mathbf{t}}^{(1)},\hat{\mathbf{t}}^{(2)})](\hat{\mathbf{t}}^{(1)}+\hat{\mathbf{t}}^{(2)},\hat{\boldsymbol{\tau}}) + \xi_{\perp}^{-1}(\hat{\mathbf{t}}^{(2)}_{\hat{\mathbf{n}}^{(1)}} + \hat{\mathbf{t}}^{(1)}_{\hat{\mathbf{n}}^{(2)}},\hat{\boldsymbol{\tau}}) + \xi_r^{-1}(s_1^2\hat{\mathbf{t}}^{(2)}_{\hat{\mathbf{n}}^{(1)}} + s_2^2\hat{\mathbf{t}}^{(1)}_{\hat{\mathbf{n}}^{(2)}},\hat{\boldsymbol{\tau}}) \tag{A3}$$

For finite h this relation determines the rotation rate of the motor $\dot{\theta}$ in terms of f. However, in the limit $h\to 0$ the motor becomes slaved to the tubules, with its orientation determined from the above relation with a zero left-hand side and irrespective of the force.

As discussed above, in this paper we consider the case of even attachment of the motor, where $s_1=s_2=s=(s_1+s_2)/2$. Simple algebra [27] shows that $\hat{\mathbf{t}}^{(2)}_{\hat{\mathbf{n}}^{(1)}}+\hat{\mathbf{t}}^{(1)}_{\hat{\mathbf{n}}^{(2)}}=[1-(\hat{\mathbf{t}}^{(1)},\hat{\mathbf{t}}^{(2)})]\times(\hat{\mathbf{t}}^{(1)}+\hat{\mathbf{t}}^{(2)})$, and in the limit $h\to 0$ we obtain the condition

$$(\hat{\mathbf{t}}^{(1)}+\hat{\mathbf{t}}^{(2)},\hat{\boldsymbol{\tau}}) = 0, \tag{A4}$$

which means that $\hat{\boldsymbol{\tau}}$ is orthogonal to the bisector of the tubules—that is, the attachment becomes symmetric. Moreover, for $h\neq 0$, even if the motor initially was not perpendicular the bisector, Eq. (A3) describes the relaxation of the motor orientation toward the angle given by condition (A4).

APPENDIX B: DISCRETIZATION

We apply the finite element method (FEM) [28] to the weak form of the governing equations (8). This allows us to treat the singular terms arising from the motor force and automatically generates appropriate natural boundary conditions.

At any time t the components of the radius vector $\mathbf{r}(t)$ and its variation $\delta\mathbf{r}(t)$ are written as linear combinations of continuously differentiable functions $\phi_{j,k}, j=0,\ldots,N-1, k=0,1$. The basis functions $\phi_{j,k}$ vanish outside the segments $[s_{j-1},s_{j+1}]$, $j=0,\ldots,N$ centered at the nodes of a one-dimensional mesh discretizing the normalized tubule $[-1/2,1/2]$ with the mesh size $\Delta s=s_{j+1}-s_j=1/N$. We construct the basis from the standard Hermite cubics: $\phi_{j,k}$ are piecewise cubic polynomials on each mesh interval and $\phi_{j,0}$ interpolate function values while $\phi_{j,1}$ interpolate derivative values. On the interval $[-1,1]$ the standard Hermite functions $\hat{\phi}_k, k=0,1$ have the form (see Ref. [28])

$$\hat{\phi}_0(s) = (|s|-1)^2(2|s|+1), \quad \hat{\phi}_1(s) = s(|s|-1)^2,$$

from which the basis functions are obtained by shifting and scaling:

$$\phi_{j,k}(s) = \hat{\phi}_k[(s-s_j)/\Delta s].$$

Similarly, the tension $g(t)$ and its variation $\delta g(t)$ are expanded by using the basis of piecewise linear "hat" functions ξ_j centered at the mesh nodes obtained from the standard hat function on $[-1,1]$:

$$\hat{\xi}(s) = 1-|s|, \quad \xi_j(s) = \hat{\xi}[(s-s_j)/\Delta s].$$

For the end nodes $j=0,N$ both ξ_j and $\phi_{j,k}$ are the suitable one-sided restrictions.

The Galerkin procedure requires that the approximate solution

$$\hat{\mathbf{r}}(s,t) = \sum_{j,k}\hat{\mathbf{r}}_{j,k}(t)\phi_{j,k}(s), \quad \hat{g}(s,t) = \sum_j \hat{g}_j(t)\xi_j(s)$$

and $\hat{\mathbf{f}}(t)$ satisfy Eqs. (10), (11) for all piecewise cubics $\delta\hat{\mathbf{r}}$, all piecewise linear functions $\delta\hat{g}$, and all scalars $\delta\hat{\mathbf{f}}$. As discussed in Sec. II B, this choice of the discretization space contains a suitable weak form of the boundary conditions (12). The resulting discrete equations can be viewed as the application of D'Alembert's principle to the energy functional (7) restricted to this finite-dimensional function space of piecewise cubic tubule conformations and piecewise linear tension profiles. The gradient flow and constraints thus generated are well-posed ordinary differential equations with discrete inextensibility and motor attachment constraints.

To write down these equations explicitly, we introduce the familiar mass and bending matrices $\mathbf{M}$ and $\mathbf{B}$, as well as a nonlinear version of the stiffness matrix $\mathbf{K}(\hat{g})$:

$$M_{j,k;j',k'} = \int_{-L/2}^{L/2}\phi_{j,k}\phi_{j',k'}ds,$$

$$B_{j,k;j',k'} = \int_{-L/2}^{L/2}(\partial_s^2\phi_{j,k})(\partial_s^2\phi_{j',k'})ds,$$

$$K_{j,k;j',k'}(\hat{g}) = \sum_i \hat{g}_i K_{i;j,k;j',k'} = \int_{-L/2}^{L/2}\phi_{j,k}\phi_{j',k'}\hat{g}_i\xi_i ds.$$

With these, the implicit Euler's scheme at a succession of times t_n produces a system of discrete equations

$$\sum_{j',k'} 2(\eta M_{j,k;j',k'}(\hat{\mathbf{r}}^{n+1}_{j',k'}-\hat{\mathbf{r}}^{n}_{j',k'})(t_{n+1}-t_n) + K_{j,k;j',k'}(\hat{g})\hat{\mathbf{r}}^{n+1}_{j',k'} + B_{j,k;j',k'}\hat{\mathbf{r}}^{n+1}_{j',k'}) + \hat{\mathbf{f}}^{n+1}\phi_{j,k}(s_a(t^{n+1})) = 0, \tag{B1}$$

$$\sum_{j,k;j',k'} K_{i;j,k;j',k'}\hat{\mathbf{r}}_{j,k}\hat{\mathbf{r}}_{j',k'} = 0, \tag{B2}$$

$$\sum_{j',k'} \hat{\mathbf{r}}_{j',k'}\phi_{j',k'}[s_a(t)] = 0, \tag{B3}$$

which are solved numerically for all i,j,k.

For our numerical studies we start with the initial state of a relaxed tubule forming a given angle $\frac{1}{2}\varphi^0$ with the vertical axis. For a given motor attachment point $s_a^0\in[-\frac{1}{2},\frac{1}{2}]$ the following discrete conformation determines a normalized symmetric tubule pair with the initial angle φ^0 and the intersection point at the origin

$$\hat{\mathbf{r}}_{j,0} = [\cos(\varphi^0/2),\sin(\varphi^0/2)](j\Delta s - s_a^0),$$

$$\hat{\mathbf{r}}_{j,1} = [\cos(\varphi^0/2), \sin(\varphi^0/2)].$$

Initially the tension and the motor force are absent $\hat{g}_i^0 = 0$, $\mathbf{f}^0 = \mathbf{0}$.

The conformation $\hat{\mathbf{r}}_{j,k}^n$ along with the tension $\hat{g}_i^n$ and the force $\mathbf{f}^n$ at a later time t_n are determined by solving the nonlinear equations (B1)–(B3) recursively. At each time t_{n+1} these equations are solved by using Newton's method with the state at time t_n serving as the initial guess. The corresponding linearized system is sparse and can be efficiently solved using any Krylov subspace method. For modest N the standard LU factorization is also feasible.

[1] J. Howard, *Mechanics of Motor Proteins and the Cytoskeleton* (Springer, New York, 2000).

[2] K. Takiguchi, J. Biochem. (Tokyo) **109**, 250 (1991).

[3] R. Urrutia, M. A. McNiven, J. P. Albanesi, D. B. Murphy, and B. Kachar, Proc. Natl. Acad. Sci. U.S.A. **88**, 6701 (1991).

[4] F. J. Nédélec, T. Surrey, A. C. Maggs, and S. Leibler, Nature (London) **389**, 305 (1997).

[5] T. Surrey, F. Nédélec, S. Leibler, and E. Karsenti, Science **292**, 1167 (2001).

[6] D. Humphrey, C. Duggan, D. Saha, D. Smith, and J. Käs, Nature (London) **416**, 413 (2002).

[7] F. Nédélec, T. Surrey, and A. C. Maggs, Phys. Rev. Lett. **86**, 3192 (2001).

[8] I. S. Aranson and L. S. Tsimring, Phys. Rev. E **71**, 050901(R) (2005).

[9] I. S. Aranson and L. S. Tsimring, Phys. Rev. E **74**, 031915 (2006).

[10] E. Ben-Naim and P. L. Krapivsky, Phys. Rev. E **73**, 031109 (2006).

[11] While it is known that NCD motors have low processivity (or typical lifetime on the microtubule), the value of the processivity is not important for the alignment process as long as density of motors is high enough: once a motor detaches from microtubule, another motor will likely bind to the same site and continue the walk. However, the important characteristic is the dwelling time at the end of the microtubule, which is expected to be significant for oligometic motor complexes used in experiments [4] [also F. Nédélec (private communication)].

[12] J. Uhde, M. Keller, E. Sackmann, A. Parmeggiani, and E. Frey, Phys. Rev. Lett. **93**, 268101 (2004).

[13] I. Goldhirsch and G. Zanetti, Phys. Rev. Lett. **70**, 1619 (1993).

[14] I. S. Aranson and L. S. Tsimring, Rev. Mod. Phys. **78**, 641 (2006).

[15] P. Ranjith and P. B. Sunil Kumar, Phys. Rev. Lett. **89**, 018302 (2002).

[16] T. Munk, O. Hallatschek, Ch. H. Wiggins, and E. Frey, Phys. Rev. E **74**, 041911 (2006).

[17] F. Gittes, B. Mickey, J. Nettleton, and J. Howard, J. Cell Biol. **120**, 923 (1993).

[18] C. Brennen and H. Winet, Annu. Rev. Fluid Mech. **9**, 339 (1977).

[19] See EPAPS Document No. E-PLEEE8-76-080710 for computer animation of simulations results of filament dynamics. For more information on EPAPS, see http://www.aip.org/pubservs/epaps.html.

[20] L. D. Landau and E. M. Lifshits, *Theory of Elasticity* (Pergamon Press, London, 1959).

[21] O. Hallatschek, E. Frey, and K. Kroy, Phys. Rev. E **70**, 031802 (2004).

[22] Y. Guo, Y. Liu, J. X. Tang, and James M. Valles, Jr., Phys. Rev. Lett. **98**, 198103 (2007).

[23] C. P. Brangwynne, F. C. MacKintosh, S. Kumar, N. A. Geisse, J. Talbor, L. Mahadevan, K. K. Parker, D. E. Ingber, and D. A. Weitz, J. Cell Biol. **173**, 733 (2006).

[24] Expression (20) is in fact similar to the critical height h_c of self-buckling condition of vertical column of density ρ and radius r, $h_c = (2.5Er^2/\rho g)^{1/3}$, where g is gravity acceleration and E Young's modulus.

[25] D. M. Smith, F. Ziebert, D. Humphrey, C. Duggan, M. Steinbeck, W. Zimmermann, and J. A. Käs, Biophys. J. (to be published).

[26] In two dimensions a vector product of a vector with $\hat{\boldsymbol{\tau}}$ is a scalar and can be replaced by a scalar product of the normal with $\hat{\boldsymbol{\tau}}$ (see illustration on the right of Fig. 14).

[27] We have $\hat{\mathbf{t}}^{(1)} + \hat{\mathbf{t}}^{(2)} = \hat{\mathbf{t}}_{\hat{\mathbf{t}}^{(2)}}^{(1)} + \hat{\mathbf{t}}_{\hat{\mathbf{n}}^{(2)}}^{(1)} + \hat{\mathbf{t}}_{\hat{\mathbf{t}}^{(1)}}^{(2)} + \hat{\mathbf{t}}_{\hat{\mathbf{n}}^{(1)}}^{(2)} = \hat{\mathbf{t}}_{\hat{\mathbf{n}}^{(2)}}^{(1)} + \hat{\mathbf{t}}_{\hat{\mathbf{n}}^{(1)}}^{(2)} + (\mathbf{t}^{(1)}, \mathbf{t}^{(2)}) \times (\hat{\mathbf{t}}^{(1)} + \hat{\mathbf{t}}^{(2)})$.

[28] G. Strang and G. Fix, *An Analysis of the Finite Element Method* (Prentice-Hall, New York, 1973).